

Chapter

COMPUTER STUDY OF THE INTERACTION OF MERCURY WITH GRAPHENE

*Alexander Y. Galashev**

Institute of High-Temperature Electrochemistry, Ural Branch,
Russian Academy of Sciences, Yekaterinburg, Russia

ABSTRACT

The contamination of natural waters and the lower atmosphere by heavy metal ions creates a serious ecological problem. Mercury is one of the most toxic heavy metals, because it is not biodegradable. We have studied the physical properties of mercury films on partially hydrogenated imperfect graphene by means of molecular dynamics at 300 K. Films prepared on the basis of three various types of the atomic interaction potential for mercury and other constant interaction potentials are considered. It is shown that the one most promising is the Schwerdtfeger potential function, at which mercury atoms do not fall into the divacancies present on graphene and atom packing with the lowest energy are realized in a liquid film and the film gradually fold into a drop. Another computer experiment has been employed to study rapid heating of a mercury film on graphene containing Stone–Wales defects. Hydrogenated edges of a graphene sheet withstand heating by 800 K. As the film contracts into a droplet, the horizontal component of the self-diffusion coefficient of Hg atoms monotonically decreases, while the vertical component passes through a deep minimum, which reflects the onset of droplet rising over the substrate. Formation of the droplet leads to a decrease in the blunt contact angle. Temperature-related changes in graphene manifest themselves as a rise in the intensity of additional peaks in the angular distribution of the closest neighbors, oscillatory pattern of the stress acting in its plane, and an almost linear growth of roughness. Molecular dynamics simulation of the bombardment of a target with a Xe₁₃ cluster beam at energies of 5–30 eV and incidence angles of 0°–60° aiming to remove a mercury film from partially hydrogenated imperfect graphene has been performed. The graphene is completely cleaned of mercury at a cluster energy of $E_{Xe} \geq 15$ eV. Mercury is removed from the graphene film via sputtering of single atoms and droplet detachment. A stress in graphene resulting from forces normal to the sheet plane is noticeably higher than that

* E-mail address: alexander-galashev@yandex.ru.

due to forces acting in its plane. Bombardment at an angle of incidence of 45° is more efficient than that at incidence of 0° and 60° and leads to lower graphene roughness. Thus, mercury can be removed from graphene by heating or bombarding with heavy noble gas clusters.

1. INTRODUCTION

Environmental pollution with heavy metals is a global problem [1, 2], due to its detrimental consequences for health [3]. Composite membranes based on graphene for the accumulation of mercury have been proposed in [4]. The structure and physical properties of liquid mercury–graphene interfaces remain unstudied; meanwhile, the prospect of using graphene as a filter demands their study. Liquids with isotropic pair interactions encounter vibrational interface structures at temperatures close to melting point T_m , providing that the T_m/T_c ratio (where T_c is the critical temperature) is low. The melting point of bulk mercury $T_m = 234$ K. Cold liquid metals such as Hg and Ga have low $T_m/T_c = 0.13$ and 0.15 , respectively.

Molecular dynamic (MD) modeling reveals their nonmonotonous density profiles near the liquid mercury/vapor interface [5]. On the other hand, the interface range has a non-zero thickness that depends on temperature. Calculating the properties of a Hg liquid–vapor interface with clear allowance for the dependence of the potential on density did not result in satisfactory agreement with the experimental data on ionic and electron density distributions orthogonal to the surface or on the reflection coefficient [6].

Theoretical study of liquids of the Hg type requires knowledge of the effective atomic potential, which allows correct predictions of the liquid/vapor phase diagram in temperature–density coordinates. Out of all the proposed potential functions for mercury, it is difficult to choose one on whose basis the structure of liquid mercury on graphene can be reproduced satisfactorily.

The structure of solid metals in contact with graphene (e.g., deposited copper films) has been studied more thoroughly [7].

Mercury absorption from smoke fumes has been studied with the use of X-ray absorption fine structure (XAFS) spectroscopy [8, 9]. XAFS spectra suggested that there is chemisorption of Hg on activated carbon. These data gave grounds to think that adsorption took place via halides, sulfides, and oxygen anions present on an activated–carbon surface. Moreover, chlorinated and bromated activated carbon was revealed with the use of X-ray absorption spectroscopy and X-ray photoelectron spectroscopy after exposure of carbon samples in smoke fumes containing Hg in an amount of $204 \mu\text{g}/\text{m}^3$ [10]. Mercury was not found on the surface of activated carbon; however, Hg–Br and Hg–Cl complexes were present. This fact underlay the assumption that sites containing Cl and Br were formed on a carbon surface prior to the capture of Hg.

The mechanism of mercury binding by activated–carbon–based sorbents was studied in [11]. It was shown that, at low Hg concentrations, it was difficult to distinguish between the mechanisms of oxidation and adsorption. The difference between them gradually grew with

Hg concentration and enhancement of Hg–Hg interaction. However, because of the close values of the bond energies in HgO, Hg₂Br₂, and HgBr₂, these surface-bound compounds were, as a rule, indistinguishable by photoelectron spectroscopy.

Liquid mercury does not wet graphite. Indeed, on highly ordered pyrolytic graphite, fresh mercury droplets have a contact angle of 152.5° [12]. As do any other liquid metals with surface tensions γ higher than 0.18 N/m, mercury does not wet carbon nanotubes [13]. The surface tension of mercury is 0.46 N/m. Nevertheless, wetting and filling of internal cavities of carbon nanotubes with mercury take place due to electrowetting [14]. The effect of electrostatic interactions on the sorption of hydrocarbons by water droplets ($\gamma_{\text{H}_2\text{O}} = 0.0729$ N/m) was shown in [15]. The mercury contact angle linearly increases with the curvature of carbon nanotube walls. Therefore, the internal surface of a nanotube has a higher phobicity with respect to mercury than the planar surface of graphene has [16]. Graphene wetting with mercury has not been studied.

Mercury is the only one of the most abundant metals that remains liquid at room temperature. The study of the adsorption of mercury at activated carbon was, as a rule, carried out experimentally. There is a limited number of theoretical studies concerning this theme.

Steckel [17] has investigated the interaction between elemental mercury and a single benzene ring in order to explain the mechanism through which elemental mercury is bound with carbon. Padak et al. [18] investigated the effect of different surface functional groups and halogens present on the surface of activated carbon on the adsorption of elemental mercury. It has been established that the addition of halogen atoms strengthens the adsorption of mercury. In [19], Padak and Wilcox have demonstrated a thermodynamic approach to the examination of the mechanism of binding of mercury and its capture in the form of HgCl and HgCl₂ on the surface of activated carbon. The energies of different possible surface complexes have been determined. In the presence of chlorine, the mercury atoms are strongly coupled to the surface. In the case of dissociative adsorption, Hg can undergo desorption, while HgCl remains on the surface. The compound HgCl₂ was not found on the stable carbon surface [20]. Understanding of the mechanism of the adsorption of mercury at activated carbon is important for the development of efficient technologies for capturing mercury.

Mercury is one of the most toxic heavy metals, and its presence is due to a combination of natural processes (volcanic activity, erosion of the mercury-containing sediments) and anthropogenic activity (extraction of minerals, pollution from the leather-dressing production and metallization of objects). Adsorption is considered to be one of the most efficient and economical methods of removing mercury from wastewater and air.

Recently, graphene membranes have begun to be used in filters for separation of trace amounts of undesirable impurities [21–23]. Repeated use of graphene in filters requires its nondestructive purification from adsorbed substances. Graphene may be purified from metals by irradiating with cluster beams of noble gases [24–29] or heating [30–33]. However, heating is reasonable to be used, when a metal has rather low boiling temperature T_b . Mercury seems to be a possible candidate for the use of this procedure. As a rule, ideal graphene is not destroyed upon heating to the boiling temperature of many metals, such as Al, Ni, or Cu, although its edges are damaged [30–32]. Graphene edges may be reinforced by

hydrogenation. Graphene treated in this way withstands cluster bombardment even at a beam energy of 30 eV [34]. It is unclear how graphene with a high concentration of Stone–Wales defects will behave, because these defects are formed before its melting [35].

The aim of this work is to choose an effective pair potential that allows reproduction of the structural, thermodynamic and kinetic properties of mercury films deposited on graphene in a molecular dynamics model. This work also studies the morphology and variations in physical properties (induced by rapid–heating) of mercury film on graphene with hydrogenated edges and high concentration of **Stone–Wales defects**. This investigation is also aimed at studying the possibility of removing adsorbed mercury from graphene via bombardment by **xenon** clusters.

2. MOLECULAR DYNAMIC MODEL

The interatomic interactions in graphene are represented by the many–body **Tersoff potential** [36]. The energy of pairwise interaction of atoms i and j taking into account the influence of other atoms (many–body effects) is written as

$$V_{ij} = f_C(r_{ij}) [A \exp(-I^{(1)} r_{ij}) - B b_{ij} \exp(-I^{(2)} r_{ij})], \quad (1)$$

$$f_C(r_{ij}) = \begin{cases} 1, & r_{ij} < R^{(1)} \\ \frac{1}{2} + \frac{1}{2} \cos[\rho(r_{ij} - R^{(1)}) / (R^{(2)} - R^{(1)})], & R^{(1)} < r_{ij} < R^{(2)} \\ 0 & r_{ij} > R^{(2)} \end{cases} \quad (2)$$

$$\begin{aligned} & r_{ij} < R^{(1)} \\ & R^{(1)} < r_{ij} < R^{(2)}, \\ & r_{ij} > R^{(2)} \end{aligned}$$

Here, r_{ij} is the spacing between the atoms i and j and the parameters A and B assign the energy characteristics of the repulsion and attraction. The many–body parameter of the bond order b_{ij} describes how the binding energy (attractive part V_{ij} of the bond) is formed during a local atomic arrangement due to the presence of other neighboring atoms. The function f_C decreases from 1 to 0 in the region of $R^{(1)} \leq r_{ij} \leq R^{(2)}$. The parameters $R^{(1)}$ and $R^{(2)}$ were selected so as to include into the consideration only nearest neighbors. The potential energy is a many–body function of the positions of atoms i , j , and k and is determined by the parameters

$$b_{ij} = (1 + b^n x_{ij}^n)^{-1/(2n)}, \quad (3)$$

$$x_{ij} = \sum_{k \neq i, j} f_C(r_{ij}) g(\mathbf{q}_{ijk}), \quad (4)$$

$$g(\mathbf{q}_{ijk}) = 1 + \frac{c^2}{d^2} - \frac{c^2}{[d^2 + (h - \cos \mathbf{q}_{ijk})^2]}, \quad (5)$$

where the parameters n , n_i , and b assign the binding force depending on the environment. The effective coordination number x_{ij} determines the average number of nearest neighbors with taking into account not only the distances between them, but also the bond angles \mathbf{q}_{ijk} . The summing up in expression (4) is conducted over all k first-order neighbors not equal to i and j . These neighbors are selected for each i - j pair and are defined at each time moment; $g(\mathbf{q}_{ijk})$ is the function of the angle between \mathbf{r}_{ij} and \mathbf{r}_{ik} where \mathbf{r}_{ij} is the vector drawn from the point of the location of the atom i to the point where the atom j is located. The parameter d assigns the width of the sharp maximum in the $g(\mathbf{q}_{ijk})$ angular dependence, the parameter c assigns the height of this peak, and the function $g(\mathbf{q}_{ijk})$ has a minimum at $h = \cos(\mathbf{q})$. All parameters of the potential were selected so as to match the theoretical and experimental data (energy of cohesion, lattice parameters, bulk moduli) for real and hypothetical graphite and diamond.

Because of the insufficiently precise determination of the force characteristics that control the C-C bonds, the Tersoff potential does not have a barrier to the rotation about the single bond. The inadequacy of the semiempirical Tersoff potential is revealed when studying the dynamic properties of graphite; it manifests in the rotation of the entire fragment to be simulated and can be corrected due by adding a torsion-like term [37]. The parameters of this potential were refined via fitting to the observed properties (standard deviations for the vibration frequencies) of graphite and diamond. The new analytical form of the potential of local torsion is given in [38]. The use in this work of weighting functions for the bond orders ensures a smooth removal of the energy of torsion connected with the dihedral angle upon any sequential break of bonds [38]. The distance $R^{(2)}$ of the covalent binding in the original Tersoff potential was limited to the value of 0.21 nm. The simulation of graphene with this potential led not only to an uncontrollable rotation, but also to the cracking of the graphene sheet [39, 40]. Therefore, we increased the value of $R^{(2)}$ to 0.23 nm and also included an additional weak attraction at $r > 0.23$ nm assigned by the Lennard-Jones (LJ) potential with the parameters used in [38].

The modeling of mercury adsorption on surface requires exact potentials of Hg-Hg and Hg-substrate interaction. Potentials presented as pair interactions are usually used to describe adsorption. The Lennard-Jones potential is the simplest of these. The parameters of this potential were chosen according to the data on the viscosity of gaseous mercury [41]. The Silver-Goldman potential (SG) is adjusted to ab initio data and provides good agreement with experimental data on spectroscopic constants [42]. The SG potential is based on the Hartree-Fock model of dispersion,

$$V_{SG}(r) = \exp(a - br - gr^2) - f_c(r) \left(\sum_{n=3}^5 \frac{C_{2n}}{r^{2n}} \right), \quad (6)$$

where

$$\begin{aligned} f_c(r) &= \exp[-(1.28r_c/r - 1)^2], \quad r < 1.28r_c \\ &= 1.0, \quad r \geq 1.28r_c. \end{aligned} \quad (7)$$

The parameters of this potential are given in [42].

The pair potential that was utilized mainly for the description of Hg - Hg interactions was proposed in [43] in the following form:

$$V_{Sch}(r) = \sum_{j=3}^9 a_{2j}^* r^{-2j}. \quad (8)$$

The authors of [43] corrected the original Schwerdtfeger (SCH) potential [44] for mercury **dimer** by scaling distances using the coefficient $I = 1.167$. The parameters a_{2j}^* represented in [43] correspond to the density of liquid Hg at $T = 300$ K. The Hg - C and Xe - Xe interactions were assigned by a Lennard-Jones potential with the parameters established in [45, 46]. The interaction between Xe atoms and the atoms of the target (Hg and C) was assigned by a purely repulsive Ziegler-Biersack-Littmark (ZBL) potential as follows [47]:

$$\begin{aligned} \Phi &= Z_i Z_j \frac{e^2}{r} \left\{ 0.1818 \exp\left(-3.2 \frac{r}{a}\right) + 0.5099 \exp\left(-0.9423 \frac{r}{a}\right) + \right. \\ &\left. + 0.2802 \exp\left(-0.4029 \frac{r}{a}\right) + 0.02817 \exp\left(-0.2016 \frac{r}{a}\right) \right\}, \end{aligned} \quad (9)$$

where Z_i and Z_j are the atomic numbers of the atoms i and j ; e is the elementary electric charge; r is the interatomic distance; and the parameter a is determined by the expression

$$a = 0.8854 a_0 (Z_i^{0.23} + Z_j^{0.23})^{-1}, \quad (10)$$

where a_0 is the Bohr radius.

We disregard the weak attraction between the atoms of Xe and Hg and also between Xe and C, since the primary purpose of this investigation is the examination of the transfer of energy and momentum, rather than of the chemical bonding [48].

The choice of interaction potential between atoms of mercury placed on graphene was carried out in the presence of divacancies in the substrate. Divacancies are one of the most widespread defects in graphene. The presence of such defects remarkably enhances the coupling of graphene with a deposited metal. In present model, nine divacancies were formed nearly uniformly on a graphene sheet. The hydrogenation of graphene results in slight surface ribbing, which also increases the linkage between metal and graphene. Preliminary partial hydrogenation strengthened the graphene edges and stabilized divacancies. A hydrogen atom was effectively added to each boundary C atom (including those in the vicinities of divacancies). More specifically, an entire CH group was considered in considering interactions, rather than individual H atoms. This group interacted with C atoms, other CH groups [49], and Hg atoms [42] through the LJ potential. Fourteen CH groups were arranged along the perimeter of each divacancy. Each group was described according to monoatomic scheme in [49]. This general scheme was designed in developing translated force fields used to predict the thermodynamic properties of complex molecules [50]. Similar hydrogenation was employed to strengthen graphene edges in cases of modeling of the mercury heating on graphene and the Xe cluster bombardment of the “mercury–graphene” target.

Stone–Wales defects along with divacancies are ones of the most widespread defects in graphene. Each Stone–Wales defect is a combination of two contiguous, five, and seven–membered rings. When heating or bombarding was investigated the graphene sheet that used to deposit Hg had six such defects approximately uniformly distributed over its surface.

A film of mercury on graphene was formed in a separate molecular dynamic calculation in two stages. At the first stage, the Hg atoms were placed above the centers of nonadjacent cells of graphene in such a way that the interatomic distance between Hg and C atoms be equal to 2.30 Å, calculated according to the density–functional method [11]. On top of this loose film consisting of 49 mercury atoms, 51 additional Hg atoms were deposited randomly. Then, the system, which consists of 100 atoms of Hg and 406 atoms of C, was brought to equilibrium in the MD calculation with a duration of 1 million time steps ($\Delta t = 0.2$ fs). For the numerical solution of the equations of motion, the Verlet algorithm was used [51]. The thus–obtained target was then bombarded with icosahedral Xe₁₃ clusters. Five starting points for the positioning of the centers of Xe₁₃ clusters were located uniformly along a line parallel to the *oy* axis (the armchair direction). This line was placed either along the left–hand edge of the graphene sheet (upon the vertical bombardment) or with an additional displacement to the left from it (upon the inclined bombardment), and was lifted to a height of 1.5 nm in the direction of the *oz* axis. The interval equal to the length of the graphene sheet in the direction of the *ox* axis (the zigzag direction) was divided into five equal sections with a length $L_i = L_x / 5$. At the beginning of every subsequent cycle of cluster impacts, the line of the starting points of the Xe₁₃ clusters was advanced a distance

L_i horizontally. As a result, the surface of the film approximated by the plane was covered with 25 evenly distributed points at which the cluster impacts were aimed. Each series included 5 cycles, or 25 impacts. At the starting point, all atoms of the Xe_{13} cluster were given the same velocity in the direction of bombardment. The clusters were sent off in turn toward the target. The lifetime (determined by the sum of the time of flight and time of interaction with the target) of each cluster was limited to 8 ps. After this time, the Xe atoms of the destroyed cluster were excluded from the consideration and a new Xe_{13} cluster began moving from another initial point. The cycle of bombardment by five clusters took 40 ps, while the series of five cycles took 0.2 ns and the entire time of bombardment (five series) took 1 ns. The clusters used for bombardments had kinetic energies of 5, 10, 15, 20, and 30 eV; the angles of incidence were 0° , 45° , and 60° .

The impact of a cluster on the surface was accompanied by heating the system. The moderate removal of the heat released from the system was performed according to the Berendsen scheme with a coupling time constant $t_c = 4$ fs [52]. The forced reduction in the temperature was conducted via the scaling of velocities v at each time step as follows:

$$v' = I v, \quad I = \left[1 + \frac{\Delta t}{t_c} \left(\frac{T_0}{T} - 1 \right) \right]^{1/2}, \quad (11)$$

where v' and v is the new and current value of velocity, respectively, I is the scaling factor, T_0 is the assigned temperature (300 K), and T is the current temperature.

The density profile of the metallic film was calculated as follows:

$$\rho(z) = \frac{n(z)\sigma_{\text{Hg}}^3}{\Delta h S_{xy} N_s}, \quad (12)$$

where $n(z)$ is the number of Hg atoms in the layer parallel to the plane of the graphene, σ_{Hg} is the effective diameter of the Hg atom, Δh is the width of the layer, S_{xy} is the area of the graphene surface, and N_s is the number of tests.

In order to calculate contact angle q between a droplet (film) surface and graphene, the largest horizontal cross-sectional area of a droplet was divided into three regions: (1) a circle with a constant area, which determines the region of the contact with graphene, (2) a ring comprising the projections of neighbors closest to region (1), and (3) an analogous ring used to reveal the external atoms of the droplet. Mercury atoms closest to the graphene surface were located in regions 1 and 2. Parameters of the procedure used for determining angles q were selected empirically. The averaging over the sizes of the rings and heights (or the number of selected Hg atoms), at which Hg atoms were located in regions 2 and 3 yielded

the average values of the horizontal and vertical coordinates used to find $\tan \mathbf{q}$. The determination of angle \mathbf{q} required averaging over time as well.

The self-diffusion coefficient was defined through the mean square of the displacement $\langle [\Delta \mathbf{r}(t)]^2 \rangle$ of the system consisting of N atoms of Hg as follows:

$$D = D_{xy} + D_z = \frac{1}{2\Gamma} \lim_{t \rightarrow \infty} \frac{1}{t} \langle [\Delta \mathbf{r}(t)]^2 \rangle_p. \quad (13)$$

Here, $\Gamma = 3$ is the dimensionality of space; $\langle \dots \rangle$ means averaging over p , where p is the number of time intervals (with the initial time t_0) for the determination of

$$[\Delta \mathbf{r}(t)]^2 = \frac{1}{N} \sum_{j=1}^N [\mathbf{r}_j(t) - \mathbf{r}_j(t_0)]^2 \text{ and } \mathbf{r}_j \text{ is the radius vector of the atom } j. \text{ Averaging is}$$

performed over five time dependences, each calculated in an interval $t = 200$ ps.

To calculate stresses that appear in graphene, the graphene sheet was divided into surface elements. The stresses $\mathbf{s}_{ua}(l)$ that appear under the action of the forces of direction \mathbf{a} ($= x, y, z$) are calculated on each element with the order number l that has the orientation u . In these calculations, products of the projections of the velocities of atoms and the projections of the forces f_{ij}^a that act on the l th element from the other atoms with the fulfillment of corresponding conditions are used as follows [53, 54]:

$$\mathbf{s}_{ua}(l) = \left\langle \sum_i^k \frac{1}{\Omega} (m v_u^i v_a^i) \right\rangle + \frac{1}{S_l} \left\langle \sum_i^k \sum_{j \neq i}^{(u_i \leq u, u_j \geq u)} (f_{ij}^a) \right\rangle. \quad (14)$$

Here, k is the number of atoms on the element l , Ω is the volume per atom, m is the mass of an atom, v_a^i is the \mathbf{a} projection of the velocity of atom i , and S_l is the area of the element l . The conditions for summation over j in the last sum in expression (14) are given in the lower and upper indices of the sum, the force that appears upon the interaction of atoms i and j goes through the l th element, and u_i is the current coordinate of the atom i (u can take values x, y, z). In the case when $u = z$, u represents the average level (height) of atoms C in graphene.

The graphene sheet had dimensions of 3.4×2.8 nm and contained 406 atoms. Each element l separated on this sheet and elongated along the axis oy (perpendicular to the zigzag direction of graphene) contained 14 C atoms and had an area of 0.68 nm^2 . Specifically, this layout corresponds to the data shown in Figure 17.

The total stresses that act in the plane of graphene were determined by summing the corresponding elementary stresses as follows:

$$S_{ua} = \sum_{l=1}^{N_l} S_{ua}(l), \quad (15)$$

where N_l is the number of surface elements.

The roughness of the surface (or the arithmetic mean deviation of the profile) was calculated as

$$R_a = \frac{1}{N_g} \sum_{i=1}^{N_g} |z_i - \bar{z}|, \quad (16)$$

where N_g is the number of sites (atoms) on the surface of the graphene sheet, z_i is the level of atom i , \bar{z} is the level of the graphene surface, and the levels z_i and \bar{z} are determined at the same time moment.

The total energy of a free one-sheeted graphene obtained at $T = 300$ K is equal to -7.02 eV, which is in agreement with the quantum-mechanical calculation (-6.98 eV) [55]. The value of the isochoric heat capacity of liquid mercury at this temperature (28.4 J/(mol K)) calculated in the MD model agrees with the experimental value of 26.9 J/(mol K).

3. CHECK OF THE Hg–Hg INTERACTION POTENTIAL FOR MERCURY DEPOSITED ON GRAPHENE

Energy $U_{\text{Hg–Hg}}$ of Hg – Hg interaction in the film, which was set after equilibrating the system with the LJ potential, was one-third that of the bond energy in a Hg_2 dimer, determined with the same potential [42]. The energies $U_{\text{Hg–Hg}}$ for three potentials with energies of mercury–graphene interaction $U_{\text{Hg–C}}$ are given in the Table 1. It can be seen the highest absolute values of energy $U_{\text{Hg–Hg}}$ were obtained for the Sch potential; the lowest, for the SG potential. On the other hand, the best cohesion between mercury and graphene was provided by the LJ potential; the worst, by the Sch potential.

Table 1. Energies $U_{\text{Hg–Hg}}$ and $U_{\text{Hg–C}}$ of a liquid mercury film on graphene for three potentials

Energy	Potentials		
	<i>LJ</i>	<i>Sch</i>	<i>SG</i>
$U_{\text{Hg–Hg}}$, eV	-0.0236	-0.0280	-0.0011
$U_{\text{Hg–C}}$, eV	-0.0154	-0.0121	-0.0148

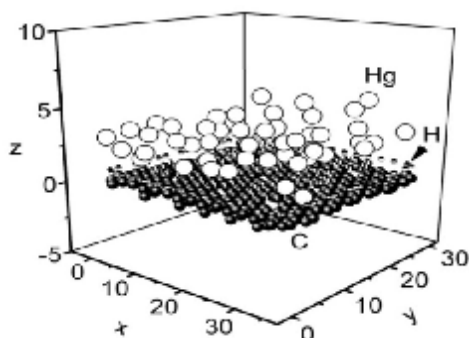


Figure 1. Configuration of a mercury film on a modified graphene system, obtained at the moment of 200 ps. The positions of H atoms correspond to the coordinates of CH-groups reduced to one point at the initial moment in time.

Using the LJ, Sch, and SG potentials for mercury yielded metal films of various structures on graphene. The LJ potential yields a denser packing of Hg atoms, while the SG potential yields more loose and uniform packing. There is a tendency toward the vaporization of atoms at temperatures as low as 300 K for the SG potential. The configuration of the H-graphene-Hg-film system obtained with the Sch potential is given in Figure 1 for the moment of 200 ps. At this time, graphene had a slight ribbing that could be detected from the deviation of boundary C atoms from the even row of H atoms built along the initial coordinates of the CH-groups. The Hg film was in this case quite uniform. However, it did not spread over the entire graphene surface; rather, it gathered into an elongated drop that was flattened to graphene. None of the Hg atoms spilled onto the other side of graphene through a divacancy, though several metal atoms did get stuck in defects. The movement of Hg atoms to the other side of the graphene was observed for two other potentials, though these spills were less than 0.08 nm long. The Sch potential was the one that was best from the viewpoint of retaining atoms on graphene.

Due to the thinness of the film, its z -profile of density was determined quite roughly and revealed no oscillations for the three types of potentials. However, the distribution of Hg atoms over the graphene surface was neither homogeneous nor uniform for the considered cases. The greatest tendency toward the formation of dense clusters in a film was characteristic for the system created using the LJ potential for mercury (Figure 2), where the first three peaks of function $g(r)$ were the highest and well resolved. A tighter and more compact structure was characteristic of the film obtained using the Sch potential: only the first four peaks of function $g(r)$ were clearly resolved. In this case, however, the Hg film was also shown to be very loose, so the first peak of function $g(r)$ shifted ~ 0.07 nm away from the position of the corresponding peak of function $g(r)$ for bulk liquid mercury [56]. The four first peaks of the film were distributed between the positions of the first and third peaks of function $g(r)$ for liquid mercury. The **radial distribution function** for the film obtained

with the SG potential had the greatest (~ 0.17 nm, relative to the position of peak of $g(r)_{liquid}$) shift of the first peak. The emergence of the second peak $g(r)$ of this film only slightly anticipated the position of the third peak of this function for the Hg film formed using the Sch potential.

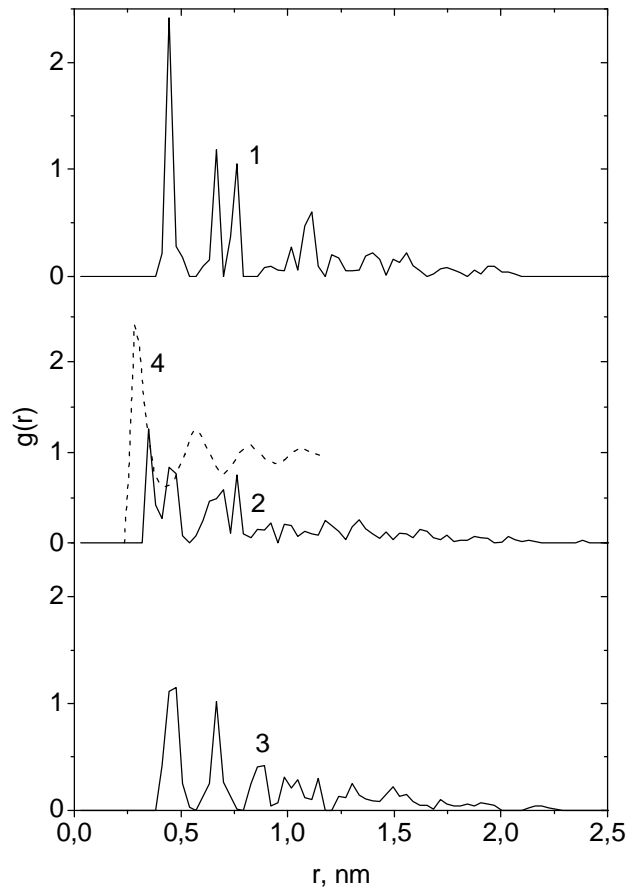


Figure 2. Radial distribution functions of mercury films on graphene, obtained with the atomic interaction potentials (1) LJ, (2) Sch, (3) SG; (4) $g(r)$ of bulk liquid mercury (MD calculations) [56].

The specificity of the geometry of system requires individual consideration of horizontal and vertical mobility of Hg atoms. The behavior of the horizontal D_{xy} and vertical D_z components of the self-diffusion coefficient of Hg when calculating at the time intervals p of 200 ps with different atomic interaction potentials for mercury is shown in Figure 3. Component D_{xy} grows only up to $p = 2$. At subsequent time intervals, D_{xy} usually stabilized or fell inconsiderably.

This behavior of D_{xy} was due mainly to the initial sealing of the Hg film and the subsequent retention of its density. The highest values of D_{xy} were obtained using the SG potential, while the lowest values were obtained with the LJ potential. The Sch potential produced most stable values of D_{xy} at $p \geq 2$. In addition, these values did not differ appreciably from the D_{xy} value obtained with the LJ potential. The vertical component of the mobility of Hg atoms behaved differently for all considered potentials. In all cases, the D_z value grew nonmonotonously along with p . Finally, the maximum value of D_z was reached with the LJ potential; the minimum value, with the SG potential. In this context, the situation is inverse to the behavior of component D_{xy} at high p . Another feature of dependence $D_z(n)$ was determined by the tendency toward vaporization from the film of Hg atoms with each potential. For all three of our model potentials, self-diffusion coefficients were obtained that were lower than the experimental value of D ($15.9 \times 10^{-11} \text{ m}^2/\text{s}$ at $T = 298 \text{ K}$) for liquid mercury [57]. Somewhat better agreement with the calculated values of $D = D_{xy} + D_z$ was achieved when D was determined via nonelastic neutron scattering on liquid mercury ($14.3 \times 10^{-11} \text{ m}^2/\text{s}$ at $T = 297 \text{ K}$) [58].

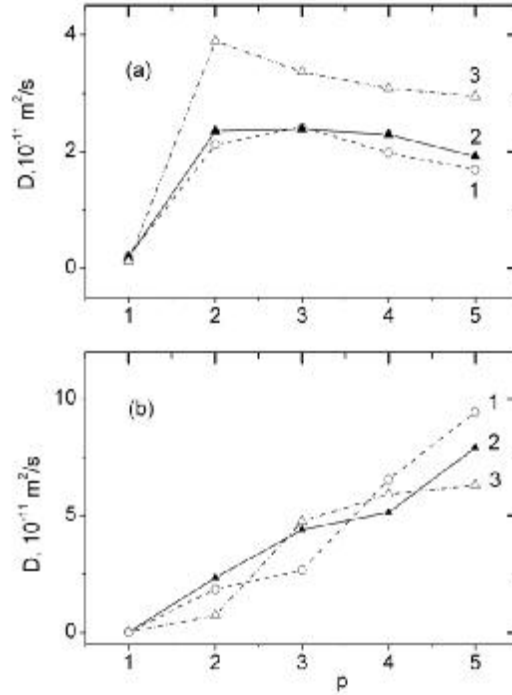


Figure 3. (a) Horizontal and (b) vertical components of the mobility coefficients of Hg atoms in mercury films on graphene, obtained using the atomic potentials (1) LJ, (2) Sch, (3) SG; p is the number of the interval in which coefficients D_{xy} and D_z were determined.

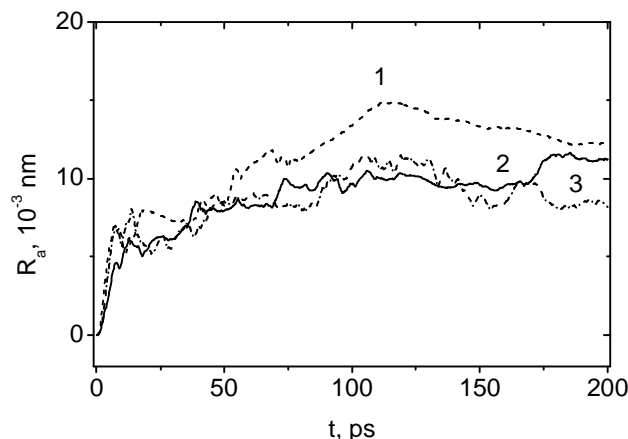


Figure 4. Evolution of the roughness of graphene coated by mercury films, obtained using the atomic potentials (1) LJ, (2) Sch, and (3) SG.

Like hydrogenation, a mercury film that forms on graphene affects its 3D structure (i.e., its roughness R_a). In calculations, the R_a value increases for Hg films that form with all three potentials (Figure 4). The highest R_a values are characteristic of graphene with a metal film obtained via Lennard Jones interaction. The Hg films created with the Sch and SG potentials have similar R_a values throughout all calculations. At the final step of calculation, however, the R_a value for the Hg film formed as the result of using the SG potential becomes lower.

4. MERCURY DROPLET FORMATION ON A GRAPHENE SURFACE

Results present in this section, obtained using the Sch potential. Taking into account the value of the time step, the calculation time, and the addend for the increase in the temperature, it is easy to show that the average rate of the system heating is $\sim 10^{11}$ K/s. Under these conditions of incomplete structural relaxation of the system, it may be superheated. In the case of metals, the superheating is aggravated by the effect of the electron subsystem, which stabilizes the condensed state. Variations accompanying the heating of a mercury film on graphene are illustrated in Figure 5. The liquid metal film begins to partly separate out of graphene already at $T = 300$ K.

This is reflected in the rise of the film edges over graphene and film thickening. The atoms of the central region of the bent Hg film are more strongly bonded to the substrate and have average minimum distance (created by 12–18 Hg atoms) = 0.28 nm. At 600 K, the Hg film is completely transformed into a droplet contacting with graphene. In this case, average distance \bar{r}_{C-Hg}^{\min} increases to 0.34 nm. A further increase in the temperature leads to a

higher rise of the majority of the droplet mass over the graphene surface. For example, at 1100 K, $\bar{r}_{C-Hg}^{\min} = 0.47$ nm.

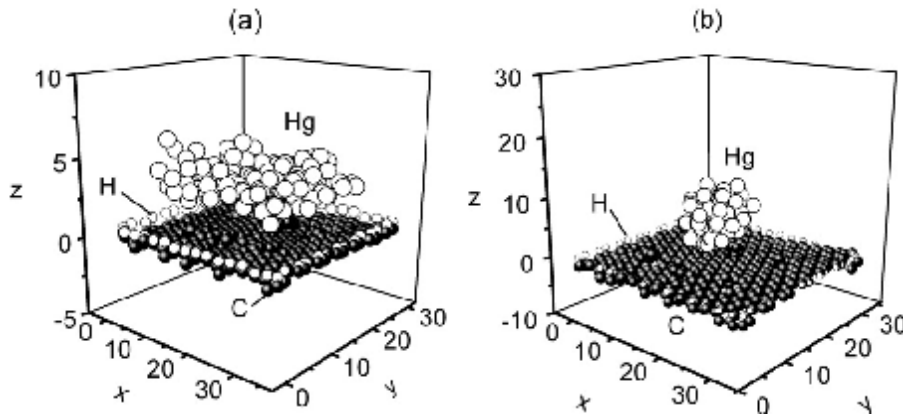


Figure 5. Configurations of the “Hg film on partly hydrogenated defective graphene” system resulting from stepwise heating at temperatures of (a) 300 and (b) 1100 K. Coordinates of atoms are given in angstroms.

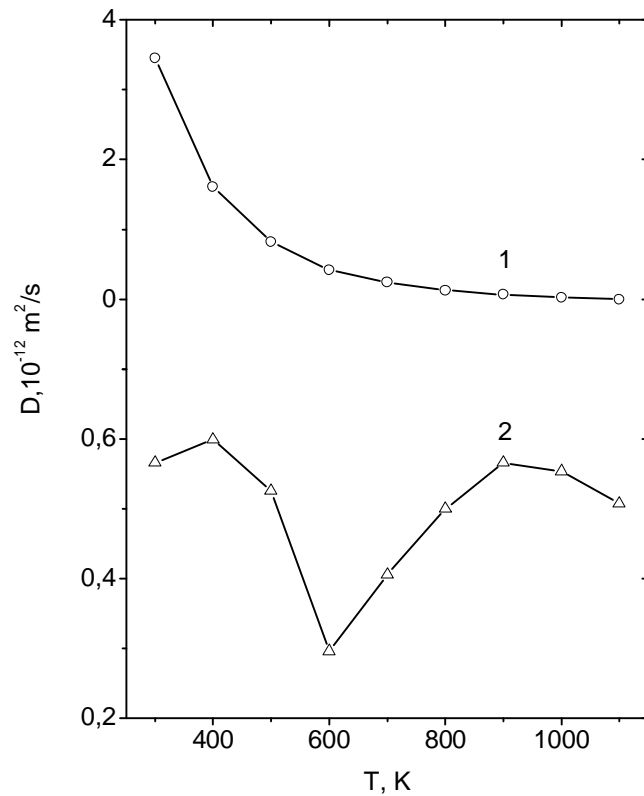


Figure 6. Temperature dependences of the (1) horizontal and (2) vertical components of the mobility coefficient for Hg atoms.

As the Hg film contracts into the droplet, horizontal component D_{xy} of the mobility coefficient of mercury atoms decreases, while vertical component D_z passes through a minimum at 600 K (Figure 6). The smooth decrease in D_{xy} characterizes the rolling of the film into a dense droplet. The behavior of component D_z indicates that the process of droplet formation ends at $T = 600$ K, and, upon a further increase in the temperature, the vertical mobility is somewhat enhanced because of a slight increase in the distance between the droplet and the graphene surface.

The extent of the transformation of the vibrational spectra of Hg atoms with the temperature increasing from 300 to 1100 K is illustrated in Figure 7. At $T = 300$ K, the spectrum of the horizontal vibrations is characterized by strong bursts diminishing with frequency. At 1100 K, the asymptotic of this spectrum remains unchanged, but the intensity of the decreasing peaks drops by six or seven times. The intensity of the vertical vibration spectrum gradually decreases down to disappearance at frequencies $\omega \geq 9.1 \times 10^{12} \text{ s}^{-1}$ irrespective of the temperature of mercury. However, as the temperature increases, the small-scale vibrations imposed onto the spectrum pattern are smoothed out. The vertical vibration spectrum is wider than the spectrum of horizontal vibrations of Hg atoms.

Vertical (scanned along the oz axis) density profiles $r(z)$ of mercury at 300 and 600 K are presented in Figure 8. The narrow $r(z)$ profile measured at $T = 300$ K has two sharp peaks, which suggest a predominantly two-layer arrangement of Hg atoms on graphene. However, at $T = 600$ K, the density profile widens and shifts upward. The low intensity of the $r(z)$ spectrum at the edges and the higher density of the intense peaks in the middle of the spectrum characterize the appearance of a spherelike formation, i.e., a droplet with a layered structure, which is evident from the large number of narrow peaks in the $r(z)$ spectrum. The very close arrangement of a number of these peaks indicates the irregularity of the formed structure.

The $g(r)$ radial distribution functions (Figure 9) plotted for the Hg atom nearest to the center of mass of liquid mercury also indicate the formation of a more compact structure at $T = 1100$ K than that at an initial temperature of 300 K. The $g(r)$ function reflects the spherically averaged structure of liquid mercury, including that in the horizontal plane, while the $r(z)$ function does not do so. A reduction in the number of peaks in the $g(r)$ function at $T = 1100$ K suggests the formation of an irregular compact structure, in which the distances to the first- and second-order neighbors are estimated to be $r_1 = 0.29$ nm and $r_2 = 0.48\text{--}0.57$ nm, respectively. The experimental values of these parameters for liquid mercury at 300 K are $r_1 = 0.31$ nm and $r_2 = 0.59$ nm [59].

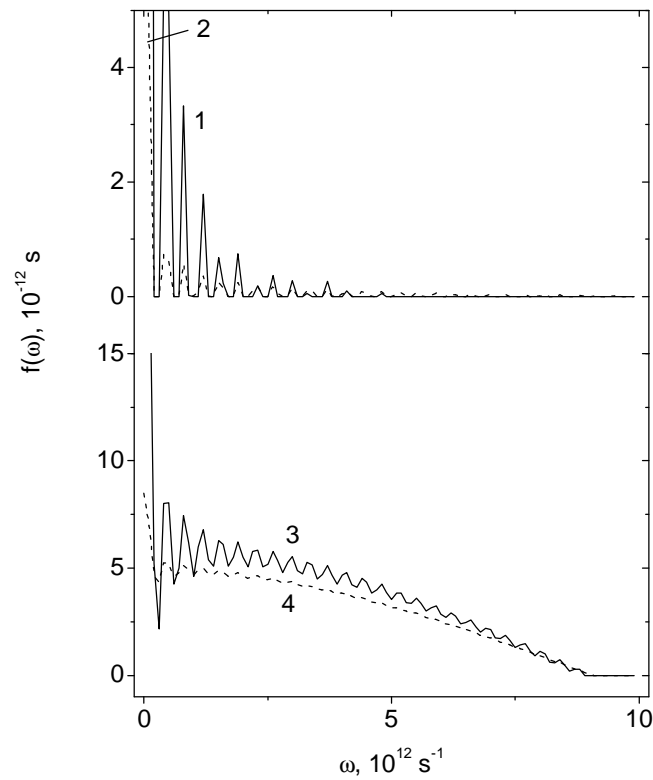


Figure 7. Frequency dependences of the (1, 2) horizontal and (3, 4) vertical components of phonon spectrum of liquid mercury on graphene measured at different temperatures: (1, 3) 300 and (2, 4) 1100 K.

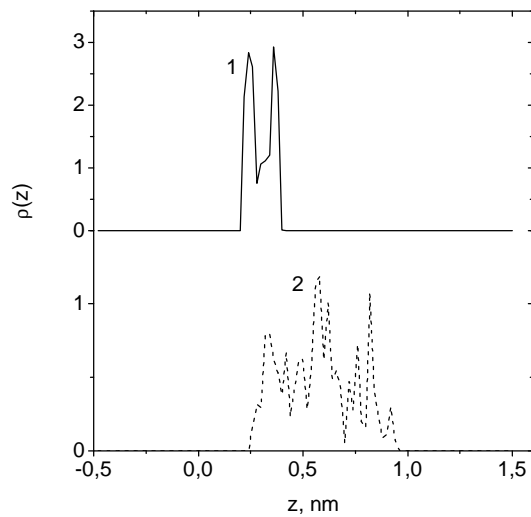


Figure 8. Vertical density profiles for liquid mercury on graphene at different temperatures: (1) 300 and (2) 600 K.

Variations in the wettability that accompany mercury film rolling into a droplet are evident from the temperature dependence of calculated contact angle q (Figure 10). An initial increase in the $q(T)$ function (up to $T = 500$ K) is due to the predominance of the influence of film heating over the effect relevant to variations in its morphology. It is known that, as the temperature increases, the blunt contact angle of a droplet becomes closer to the flat angle. In spite of a noticeable rise of the droplet over graphene, which begins from 600 K, its separation from the substrate may only be related to a temperature of 800 K. The calculation at 600 K ends when seven Hg atoms are still located at distances r from graphene shorter than distance $r_{\min} = 0.3727$ nm corresponding to the minimum of the LJ potential describing the Hg–C interactions. At 700 K two such cases are observed, while, at $T = 800$ and 900 K, none take place. However, one and two Hg atoms with $r < r_{\min}$ arise at $T = 1000$ and 1100 K, respectively. Average angle $\bar{q} = 127.1^\circ$, which corresponds to temperatures of 900–1100 K, may be considered to be the contact angle of a 100–atom cluster of Hg on graphene. This angle is noticeably smaller than the contact angle for a macroscopic droplet of mercury on pyrolytic graphite (dashed line in Figure 10) [16]. This agrees with the common ideas of a reduction in angle q with a decrease in the droplet radius. The inset of Figure 10 shows the time dependence of q at 600 K. It can be seen that angle q has begun to noticeably decrease by the end of the calculation at this temperature.

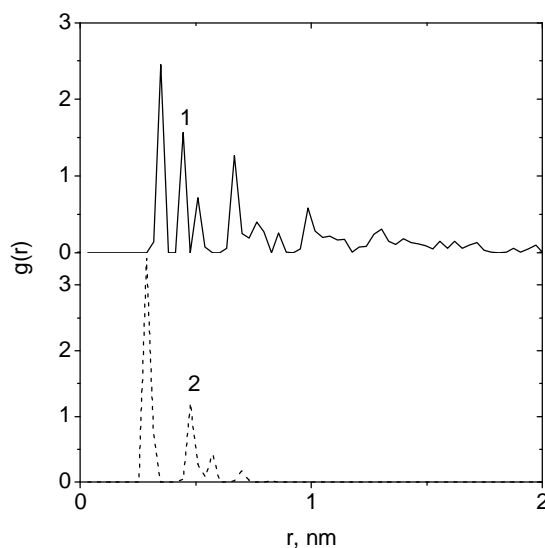


Figure 9. Radial distribution functions calculated for liquid mercury on graphene at different temperatures: (1) 300 and (2) 1100 K.

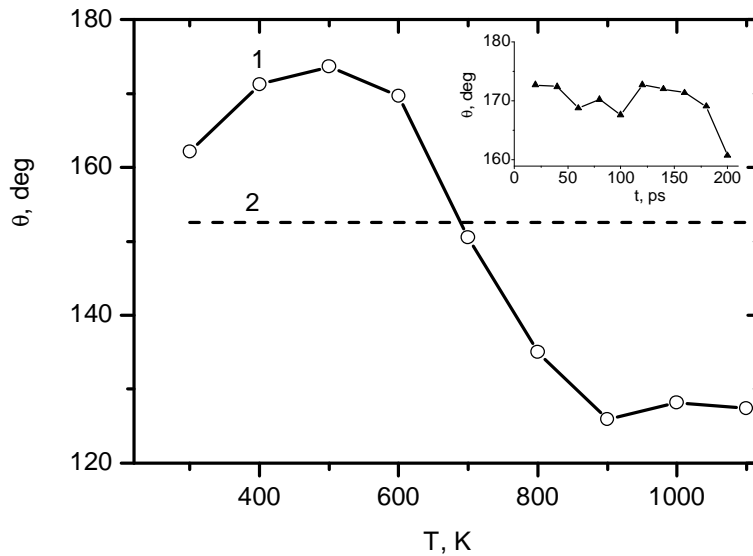


Figure 10. Temperature dependences of contact angles for (1) mercury on graphene and (2) macroscopic mercury droplet on pyrolytic graphite [16]. The inset shows the temperature dependence of contact angle for a mercury droplet on graphene at $T = 600$ K.

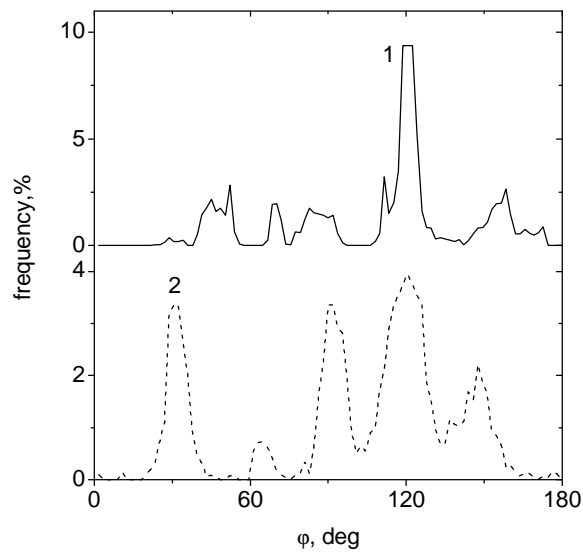


Figure 11. Angular distributions for nearest neighbors in graphene at a high concentration of Stone–Wales defects and different temperatures: (1) 300 and (2) 1100 K.

A peak at 120° , which indicates the presence of the main elements of the two-dimensional structure, i.e., hexagonal honeycombs, dominates in the angular distribution of the nearest neighbors in graphene at $T = 300$ K (Figure 11). Additional peaks arise in this distribution due to the high density of the Stone–Wales defects (penta- and heptagonal cells). In spite of the fact that 1100 K is not a high temperature for graphene (its melting temperature

is $T_m = 4900$ K), its structure has already suffered from obvious changes. The peak at 120° C has become significantly wider. Moreover, the intensities of peaks at 30° , 90° , and 148° have substantially increased.

These changes indicate the growth of the defects in the graphene structure at $T = 1100$ K. Stresses S_{zx} and S_{zy} , which characterize the action of the internal horizontal forces in the grapheme plane have close values, which weakly vary with an increase in the temperature (Figure 12). A noticeable difference between these stresses, which is observed at $T = 300$ K, disappears while approaching a temperature of 500 K. The values of stress S_{zz} , which characterizes the action of the vertically directed forces, have the same order of magnitude as stresses S_{zx} and S_{zy} have. The $S_{zz}(T)$ function comprises two regions of the most rapid variations, i.e., a decrease upon heating to 400 K and an increase upon heating after 1000 K. The lowest values of S_{zz} are observed in a temperature range of 600–800 K, in which the majority of the droplet mass rises over graphene.

Roughness R_a of graphene saturated with the Stone–Wales defects rapidly increases with temperature (Figure 13). As a result of vertical bombardment by Xe_{13} clusters with an energy of 30 eV, graphene containing vacancies and coated with a mercury film acquires a roughness, which is close to R_a at 400 K without the bombardment [34]. The strong bond between carbon atoms in graphene is better preserved at a high temperature ($T \geq 1000$ K), when the simulation is performed in terms of the Sch potential than within the framework of the SG potential.

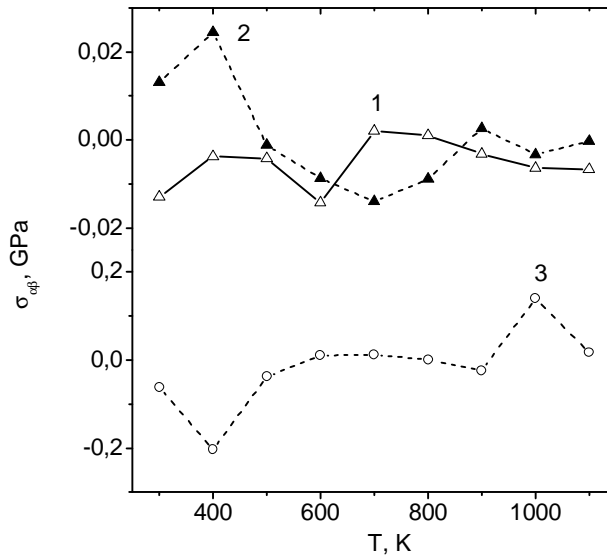


Figure 12. Temperature dependences of the components of the stress tensor in the plane of a mercury-coated defective graphene sheet: (1) σ_{zx} , (2) σ_{zy} , and (3) σ_{zz} .

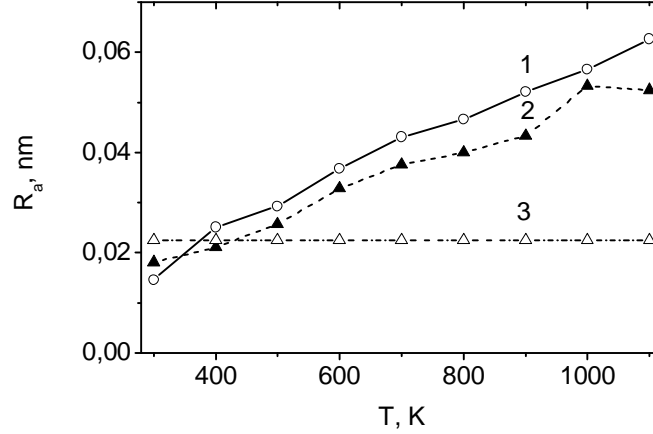


Figure 13. Temperature dependences of roughness coefficient for mercury-coated graphene with regard to Hg–Hg interactions plotted with the use of different models: (1) SG potential and (2, 3) Sch potential. Temperature is varied by means of (1, 2) heating and (3) vertical bombardment by Xe₁₃ clusters with an energy of 30 eV.

5. THE XENON CLUSTER BOMBARDMENT OF MERCURY ON GRAPHENE

In this section we consider the behavior of the mercury film on graphene when the Hg – Hg interaction is based on the Schwerdtfeger interaction potential. The cluster bombardment using 125 impacts with an angle of incidence of 0° did not lead to any significant removal of mercury from graphene at all energies of Xe₁₃ clusters in the range of 5–30 eV. As a rule, more than half of the Hg atoms after the completion of the bombardment were bound with graphene, as before. The variations in the principal components (σ_{xx} , σ_{yy} , and σ_{zz}) of the stress tensor for the Hg film located on graphene under the action of 5–eV cluster impacts is shown in Figure 14. In the case of structured media, the pressure tensor is not necessarily symmetric, because the extrinsic angular momentum can transform into the intrinsic one, and vice versa. Here, only the total angular momentum must be conserved. In the first approximation, the liquid–metal film on a solid surface can be regarded as a viscous liquid. Successive Xe₁₃ cluster impacts force this liquid to move. In this case, the stress tensor is defined as [60]

$$\sigma_{\alpha\beta} = -P\delta_{\alpha\beta} + \sigma'_{\alpha\beta}, \quad (17)$$

where $\sigma'_{\alpha\beta}$ is the viscous stress tensor.

The closeness of the functions $\sigma_{xx}(t)$ and $\sigma_{yy}(t)$ (Figure 14) indicates very small values of σ'_{xx} and σ'_{yy} . At the same time, the function $\sigma_{zz}(t)$ differs significantly from the

functions $\sigma_{xx}(t)$ and $\sigma_{yy}(t)$. This is related to the fact that graphene hinders motion in the vertical downward direction. The effective σ'_{zz} turns out to be very large (compared with P). Large oscillations of the function $\sigma_{zz}(t)$ are also related to the presence of graphene reflecting Hg atoms upward after each collision with Xe atoms. It can be seen that the relaxation of stresses σ_{xx} and σ_{yy} occurs faster than the decrease in the stress σ_{zz} .

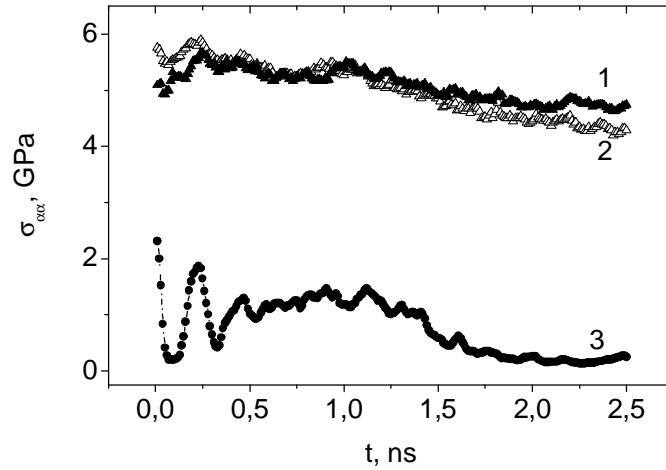


Figure 14. Time dependence of the diagonal stress tensor components (1) σ_{xx} , (2) σ_{yy} , and (3) σ_{zz} for the Hg film on graphene subjected to 5-eV Xe_{13} cluster bombardment.

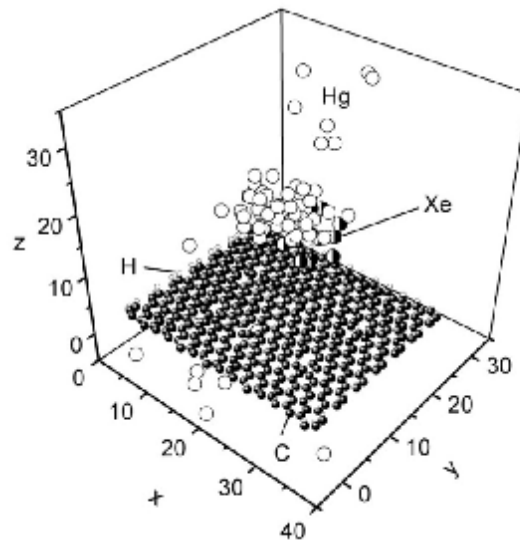


Figure 15. Configuration of a system consisting of a mercury film on a partially hydrogenated imperfect graphene sheet after bombardment by a beam of Xe_{13} clusters at the angle of incidence of 60° and the energy equal to 10 eV. The coordinates of atoms are given in angstroms.

The bombardment at the angle of incidence equal to 45° was considerably more successful. In this case, beginning with the energy of beam equal to 15 eV, graphene was almost completely cleaned of mercury. Only single atoms could remain connected with the graphene sheet; moreover, the majority of these atoms were retained at the edges of the sheet. The remaining atoms of Hg were scattered far beyond the limits of the graphene sheet predominantly in two directions (in the horizontal direction at a sharp angle to the axis ox , and upward). As a rule, the Hg atoms were knocked out from the film one by one and less frequently in the form of dimers and trimers. However, at the energies of the cluster beam $E_{Xe} \geq 15$ eV there was always separated also a drop of mercury from graphene. An increase in the angle of incidence of the Xe_{13} clusters to 60° led to the removal of mercury from graphene upon the energy of the beam of 10 eV (Figure 15). A subsequent increase in the energy of the cluster beam at $q = 60^\circ$ did not give a desired result: graphene was not cleaned of mercury.

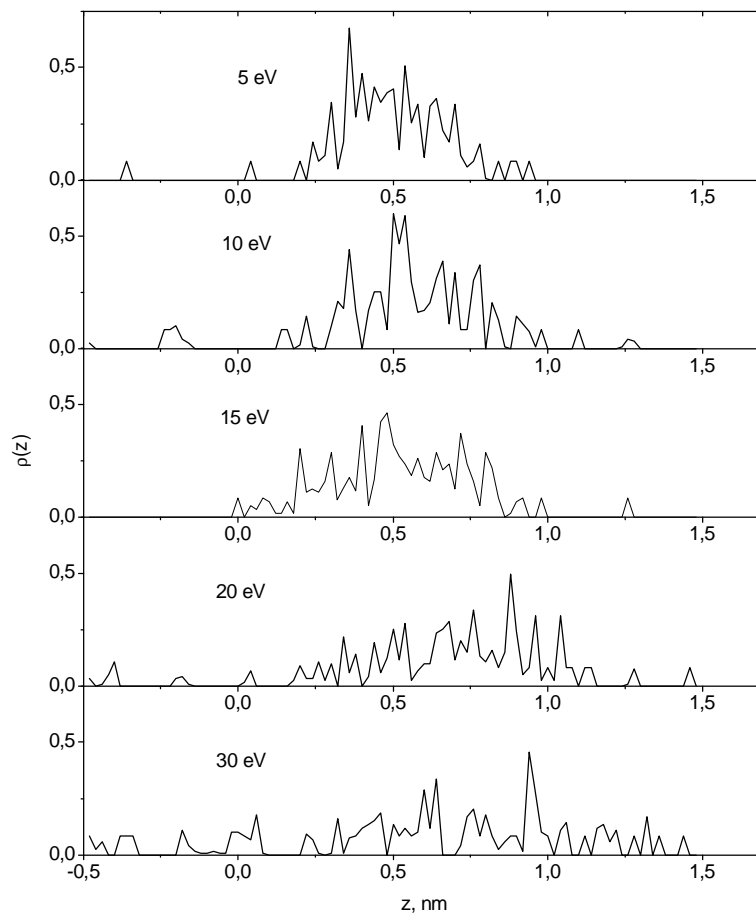


Figure 16. Vertical profiles of the density of liquid mercury on graphene. Numbers (eV) indicate the energies of the falling clusters.

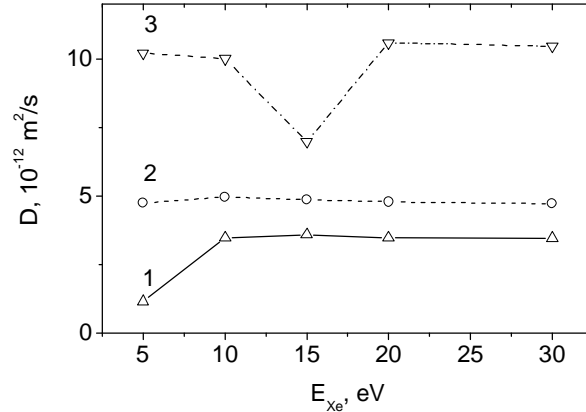


Figure 17. Self-diffusion coefficients of Hg atoms calculated for the cases of bombardment of the target at the angles of incidence (1) 0° , (2) 45° , and (3) 60° depending on the energies of the cluster beam E_{Xe} .

The vertical profiles of the mercury density reflect the displacement of the atoms of metal predominantly upward as a result of the cluster bombardment of the target at the angle of incidence of clusters equal to $\mathbf{q} = 0^\circ$ (Figure 16). The maximum of the density profile is consecutively displaced upward with an increasing energy of the bombarding clusters. A delay in this motion is observed only at $E_{Xe} = 15$ eV, where the position of the density maximum deflected slightly to the reverse side in comparison with the position for the profile at $E_{Xe} = 10$ eV. However, already at $E_{Xe} = 20$ eV the position of the maximum density substantially increased in height and continued increasing at $E_{Xe} = 30$ eV. The density profiles at $E_{Xe} \geq 20$ eV increase their vertical extents in both directions (upward and downward).

With an increase in the angle of incidence of the xenon clusters, there occurs an increase in the self-diffusion coefficient of mercury atoms; especially, this is noticeable on going from the angle $\mathbf{q} = 45^\circ$ to the angle of 60° . The lowest value of the self-diffusion coefficient of Hg atoms is observed upon the vertical bombardment with the energy of Xe_{13} clusters equal to 5 eV (Figure 17). At energies $E_{Xe} \geq 10$ eV and at an angle of incidence $\mathbf{q} = 0^\circ$, there is a very weak dependence of the self-diffusion coefficient on the energy of the falling clusters. A similar weak dependence is manifested in the entire range of cluster energies at the angle of incidence $\mathbf{q} = 45^\circ$. At the angle $\mathbf{q} = 60^\circ$, the $D(E_{Xe})$ function has a deep minimum at 15 eV. The origin of this minimum is most likely connected with the fact that it occurs upon bombardment with precisely such energy of clusters that the most rapid rolling of the mercury film into a drop occurs, from which the Hg atoms can be kicked out only with difficulty. Except for this specific feature, no significant changes in the behavior of the coefficient of self-diffusion is observed upon the variations in the energy with an angle of incidence $\mathbf{q} = 60^\circ$. The weak change in the $D(E_{Xe})$ function indicates the effective removal of heat that is separated upon the impacts using the Berendsen thermostat. In other words, the energy is not accumulated in the system in the course of the bombardment.

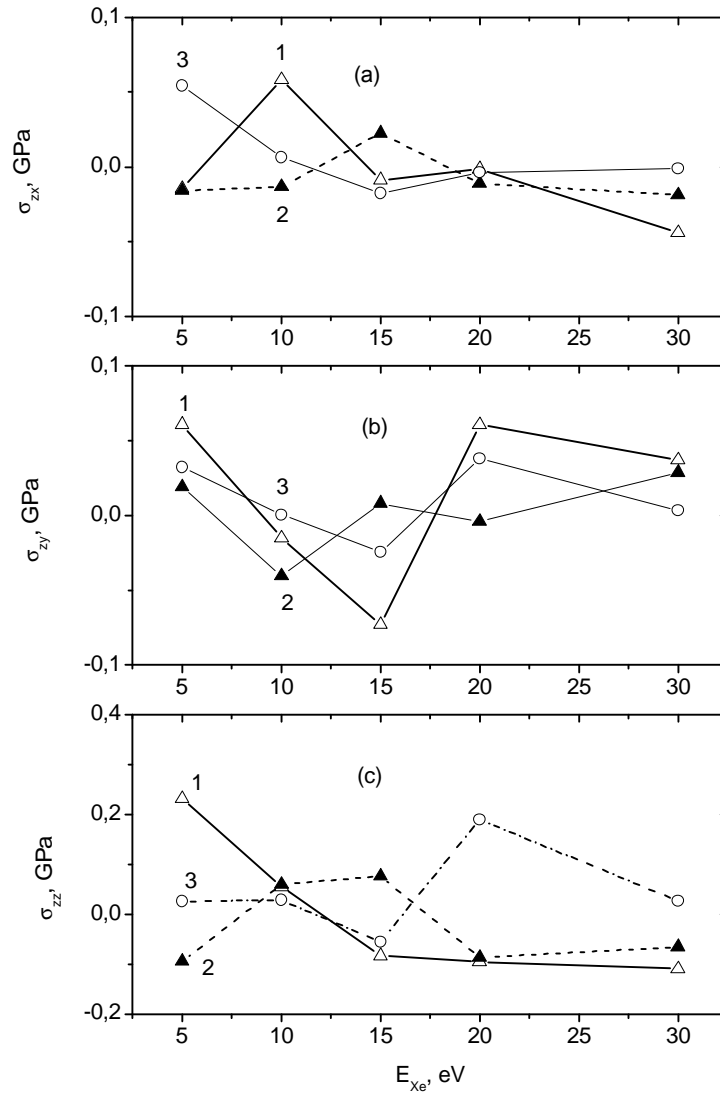


Figure 18. Components of the stress tensor in graphene ((a) σ_{zx} , (b) σ_{zy} , (c) σ_{zz}) obtained for the cases of the bombardment of targets at the angles of incidence (1) 0° , (2) 45° , and (3) 60° depending on the energies of the cluster beam E_{Xe} .

The $S_{ab}(E_{Xe})$ dependences of the stresses in the plane of graphene caused by horizontal (Figures 18a, 18b) and vertical (Figure 18c) forces exhibit a complex behavior, which is different for the different angles of incidence. As a rule, the stresses S_{zz} created by vertical forces are noticeably higher than the stresses S_{zx} and S_{zy} that appear due to the action of horizontal forces. At cluster energies E_{Xe} that lead to the detachment of the majority of Hg atoms from graphene, the stress S_{zz} has relatively low values. Recall that

this occurs at energies $E_{Xe} \geq 15$ eV at an angle of incidence of 45° and at $E_{Xe} = 10$ eV at the angle $q = 60^\circ$.

The roughness R_a of graphene increases continuously in the course of cluster bombardment. The inset in Figure 19 gives a representation of the variation of the function $R_a(t)$ in time in the case of bombardment with an energy of Xe_{13} clusters equal to 15 eV at the angle of incidence of 0° . The bombardment has a significant effect on the roughness of graphene. The magnitude of R_a increases by 20–40%, even as a result of the bombardment with the energy of clusters equal to only 5 eV; the effect is strongest at an angle of incidence of 60° . The form of functions $R_a(E_{Xe})$ obtained at different values of the energy of the Xe_{13} clusters is shown in Figure 19. It can be seen that bombardment at an angle of $q = 45^\circ$ leads to the lowest values of R_a . Thus, after this bombardment at an energy of the beam equal to 30 eV, the value of R_a proves to be below the appropriate characteristics that correspond to the angles of incidence of 0° and 60° by 9.6% and 11.8%, respectively.

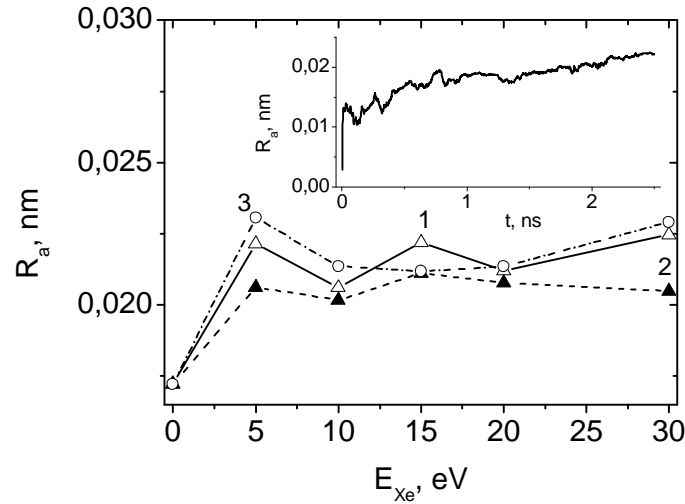


Figure 19. Roughness of graphene obtained as a result of the bombardments of the target at the angles of incidence (1) 0° , (2) 45° , and (3) 60° at the energies of the cluster beam E_{Xe} . Inset shows the change in the roughness of graphene in the course of the bombardment of the target by Xe_{13} clusters at the angle of incidence equal to 0° and at an energy of the cluster beam of 15 eV.

DISCUSSION

Variations in the state of a liquid under a real regime may lead to its superheating, i.e., the existence of the liquid above the boiling temperature upon evaporation. A liquid is superheated as a result of either a rapid heating at a constant pressure or a rapid loss of sealing at a constant temperature. In any case, the liquid enters the region of a nonequilibrium or metastable state, in which its temperature becomes higher than the saturation temperature at

normal pressure. The degree of superheating for nonmetal liquids may be as high as several hundred degrees and depends mainly on the rate of heating or reduction in pressure. In the limiting case of complete absence of vapor, very high degrees of superheating may be reached. The superheating is eliminated via an instantaneous change in the phase state, such as explosive boiling up. A high superheating of a liquid is limited by homogeneous nucleation. The ultimate superheating that has been reached for water is (329–333) K [61, 62]. Therewith, a critical nucleus contained nearly 20 molecules [63]. Phase transitions in metal-based systems are distinguished by some specific features. In this case, the electronic and molecular structures of liquid and vapor phases occurring at equilibrium are greatly different. For example, liquid mercury and cesium at temperatures close to their ordinary melting points are considered to be normal liquid metals having properties typical of a condensed state. Slight changes in the main properties, such as electrical conductivity or magnetic susceptibility as a result of melting show that the electronic structure of the liquid is similar to that of a crystalline solid. This behavior is commonly explained by the fact that the short-range atomic correlations in a small volume are analogous for a liquid and a crystal. In addition, the ion charges in metals are strongly screened by conduction electrons; therefore, the long-range order of ion potentials is of no importance for either a liquid or a solid. The unusual behavior of a metal-based system is evident from the metal–nonmetal transition, which takes place upon the evaporation of a dense liquid, i.e., when it passes into a rarefied vapor, or in the case of liquid expansion upon heating. The low surface free energy of the majority of nonmetal solids excludes their wettability with inert (nonreactive) liquid metals. However, for mercury located on glass, quartz, or sapphire, a prewetting transition is distinctly observed. The existence of the **metal–nonmetal transition** noticeably affects the thermodynamic, structural, interfacial, and dynamic properties of metals. The conductivity–density dependence for bivalent mercury may be divided into three regions.

Mercury is a polyvalent metal, which is available for studying in the liquid state at low temperatures. The critical point of its vapor is characterized by the following parameters: $T_c = 1751$ K, $P_c = 167.3$ MPa, and $r_c = 5.8$ g/cm³. Mercury has the lowest critical temperature of those known for all liquid metals. This fact is of importance from the point of view of precise measurement of physical properties at high temperatures and pressures.

The experimental data on droplet evaporation on a hot surface indicate the existence of a discontinuity in the dependence of temperature difference $\Delta T = T_{\text{vap}}^i - T_{\text{liq}}^i$ (i denotes the interface) on vapor pressure P_{vap}^i [64, 65]. At a liquid–vapor interface, the temperature is always higher on the side of the vapor. This is explained by the fact that high-energy molecules are primarily evaporated, while molecules with lower energies remain in the droplet. A reduction in the flux of molecules to the vapor phase is mainly observed at high temperatures – for water, at $T/T_c \approx 0.84$ [66]. The value of the temperature discontinuity for water may be higher than 1400 K [66]. Mercury atoms are 11 times heavier than water molecules. Mercury is characterized by another type of interaction. It may be thought that a mercury droplet remains stable at high temperatures because of a reduction in the flux of Hg atoms to the vapor phase; however, the characteristic features of this process differ from the behavior of water.

The high **stability** of a model mercury droplet may also be explained as follows. The interaction potential between two mercury atoms is, as a rule, considered to be a potential between highly polarizable closed shells, which permit very low migration of electron density from one partner to another; i.e., this potential is, to some extent, similar to a potential function that describes the interaction between atoms of noble gases. We have proven (using the Sch potential) the formation of a mercury droplet on graphene upon rapid heating using a calculation similar to that reported here, but performed in terms of the SG potential.

In [67], it was noted that the model approximations that use pair interaction potentials to describe the liquid–gas transition for mercury are rough [67]. Experimental gas–liquid coexistence curves may be precisely reproduced, provided that the two–atom curves obtained for potential energy from the former principles are supplemented with the many–body potential, which describes the associative interaction of an atom with neighboring atoms that altogether form a virtual cluster. The liquid–gas transition for mercury is distinguished by the fact that the local electronic states change from metal to nonmetal ones because of weakened many–particle interactions and decreased average coordination numbers.

According to the calculation in terms of the Sch potential, Hg film rolls into a droplet upon heating. By the end of the calculation at 600 K, an almost spherical droplet is formed on graphene, with the droplet remaining near the graphene surface even at 1100 K. When the SG potential function is used, the distance between the droplet and graphene rapidly increases up to a temperature of 1000 K. No significant separation of Hg atoms from the droplet takes place in this case. Most likely, the Sch and SG potentials give an overestimated indirect effect of the electron component on the Hg – Hg interaction, which leads to the high stability of liquid mercury with respect to its vapor.

It is of interest to compare the results of the study of the removal of films of copper and lead by the bombardment with clusters of rare gases with the present investigation of the **purification** of graphene from mercury. First of all, the different mechanisms of the detachment of these heavy metals from graphene during the irradiation of the target by a cluster beam should be noted. In the case of the bombardment of the copper film with Ar₁₃ clusters, separate Cu atoms are knocked out [24–29]. No regime of bombardment led to the separation of fairly large fragments of the Cu film from graphene. When the lead film is bombarded, separate atoms are also knocked out, but the prevailing mechanism of the removal of the metal from graphene is the separation of islands of a Pb film from the substrate [34]. Since it was only detached away graphene, the island experiences a transformation from a two–dimensional to a three–dimensional structure; otherwise, mercury is separated from graphene. The unique behavior of mercury is due to its liquid state and the poor wetting of graphene; as a result, the Hg film has a tendency to roll into a drop. For this reason, both separate atoms and droplets of significant size are separated from graphene in the course of bombardment. Let us emphasize that it is precisely a drop that is torn off, rather than an island with a two–dimensional morphology. There are several other differences in the processes of the removal of the film of heavy metals from graphene. Thus, the film of copper is not completely removed from graphene, even at an energy of the beam equal to 30 eV at angles of incidence of 0° and 60° [24], and the most efficient method is **removal** using cluster bombardment at an angle $q = 45^\circ$. In the case of lead, the most efficient procedure can be

considered to be **irradiation** by a cluster beam at the angles of incidence of 0° and 60° . In this case, graphene was completely cleaned of metal at energies of the beam equal to 10 and 15 eV. Complete cleaning was also achieved at an angle $\theta = 45^\circ$, but the energy of the cluster beam required in this case was equal to 20 eV. The greatest effect from the bombardment of the mercury-on-graphene target is obtained at an angle of incidence equal to 45° . At this angle of incidence, graphene is cleaned of Hg at all energies $E_{xe} \geq 15$ eV. A less stable cleaning effect was achieved at an angle of incidence of 60° . In the case of an angle of incidence equal to 0° , no significant removal of mercury from graphene occurs in the range of energies of the **beam** equal to 5–30 eV. Thus, the removal of different heavy metals requires different conditions for bombardment and occurs via different mechanisms.

To check the correctness of the results, we also conducted calculations with another pair potential for mercury and another potential that describes the mercury-graphene interaction. The Hg–Hg interactions were determined based on applying the potential proposed by Silver and Goldman with the parameters given in [42]. Here, we obtained results close to those where the Sch potential served as the potential function for mercury. In the calculations that applied the SG potential, upon bombardment, the Hg film was more rapidly transformed into the drop and was separated from graphene. The complete removal of mercury from graphene was only achieved at an angle of incidence equal to 45° at $E_{xe} \geq 15$ eV. When using a Morse potential with the parameters given in [68] for the representation of Hg–C interactions, mercury upon the bombardment was separated from graphene more difficultly, and the complete cleaning at the angle $\theta = 45^\circ$ was achieved at the energies $E_{xe} \geq 20$ eV.

CONCLUSION

The forces of **cohesion** between mercury and graphene atoms are weak, compared to the ones between mercury atoms. Mercury tends towards its natural boundary angle while wetting decreases and mercury gradually consolidates into individual drops. This phenomenon is largely reproduced using the Sch potential. A tendency toward drop formation is also observed for the LJ and SG potentials, but in these cases there are considerably more individual atoms on the graphene surface, and each drop has a less distinct profile. For real mercury, **vaporization** proceeds at temperatures above 291 K. Cohesion with modified graphene does not allow Hg atoms to detach from the film at distances much greater than atomic ones at 300 K. However, the tendency toward the vaporization of Hg atoms is still observed in model systems and is clearer when using the SG potential.

Molecular dynamics has been employed to study the stepwise heating of a mercury film on imperfect graphene. A graphene sheet with a high concentration of Stone–Wales defects and hydrogenated edges has been examined. An increase in temperature has been shown to cause gradual **rolling** of the film into a droplet and a slow movement of the droplet away from graphene. The horizontal component of the mobility coefficient of Hg atoms smoothly decreases in the course of this process, while the vertical component nonmonotonically increases after a reduction reached by a temperature of 600 K. As a whole, the spectra of the

horizontal and vertical vibrations of Hg atoms similarly vary with a rise in the temperature; i.e., the small-scale thermal fluctuations in the spectra are smoothed. The vertical profile of mercury density shifts upward and widens to a size that corresponds to the diameter of the formed liquid metal droplet. The formation of the mercury droplet is accompanied by a reduction in the domain of the radial distribution function and a decrease in the number and intensity of pronounced peaks of the $g(r)$ function. An increase in the temperature accelerates the formation of the droplet and decreases the contact angle. In the angular distribution of nearest neighbors, the intensity of the main peak at 120° , which reflects the hexagonal cells, decreases, while intense peaks corresponding to angles of 30° , 90° , and 148° arise. The stresses in the graphene plane that are caused by the horizontal and vertical forces have close magnitudes in the considered temperature range. Graphene roughness rapidly grows with temperature, reaching a maximum value at 1000 K. Hydrogenated graphene edges are not damaged significantly upon heating to high temperatures. Thus, upon rapid heating, a mercury film on graphene is transformed into a droplet with substantial changes in atomic packing and physical properties.

The behavior of a system of mercury-on-partially-hydrogenated-graphene has been investigated under irradiation by a beam of Xe_{13} clusters with energies of 5–30 eV at angles of incidence equal to 0° , 45° , and 60° . Over a wide range of energies ($E_{\text{Xe}} \geq 15$ eV), the almost complete removal of mercury from graphene was only achieved at an angle of incidence of 45° . The film of mercury, which has a tendency to become rolled up into a drop, is separated from graphene in the form of single atoms, dimers, trimers, and spherical droplets. In the course of the bombardment, mercury exhibits a weak cohesion with graphene. With an increase in the energy of the falling clusters from 5 to 30 eV, the $\Gamma(z)$ profile evolves in a complex way, demonstrating the formation of a drop of mercury on graphene, as well as the formation of a vapor of Hg monomers. The smallest change in the components of the mobility of Hg atoms upon the variation of the energy of the cluster beam occurs at an angle of incidence equal to 45° . At the energies of the cluster beam under consideration, the stresses in the plane of graphene caused by vertical forces noticeably exceed the stresses created by the horizontally directed forces, regardless of the angle of incidence. The roughness of graphene increases noticeably in the course of cluster bombardment. The lowest roughness is demonstrated by graphene subjected to irradiation by the beam of clusters with an angle of incidence equal to 45° . The hydrogenated edges of graphene do not suffer noticeable damages at all the energies investigated and at all the angles of incidence of the bombarding clusters.

REFERENCES

- [1] Merian, E. *Metals and their compounds in the environment: occurrence, analysis and biological relevance*; VCH Publishers: Weinheim, US, 1991; p. 1438.
- [2] Fernandez-Leborans, G. H.; Yolanda, O. *Ecotoxicology Environmental Safety* 2000, 47, 266–276.
- [3] Sayari, A.; Hamoudi, S.; Yang, Y. *Chem. Mater.* 2005, 17, 212–216.

-
- [4] Li, R.; Liu, L.; Yang, F. *Chem. Eng. J.* 2013, 229, 460–468.
- [5] Bomont, J.-M.; Bretonnet, J.-L. *J. Phys.: Conference Series* 2008, 98, 042018.
- [6] Bomont, J.-M.; Bretonnet, J.-L.; Gonzalez, D. J.; Gonzalez, L. E. *Phys. Rev. B* 2009, 79, 144202.
- [7] Galashev, A. Y.; Polukhin V. A. *Rus. J. Phys. Chem. A* 2014, 88, 995–999.
- [8] Lee, C. W.; Serre, S. D.; Zhao, Y.; Lee, S. J.; Hastings, T. W. *J. Air & Waste Manage. Assoc.* 2008, 58, 484–493.
- [9] Huggins, F. E.; Yap, N.; Huffman, G. P.; Senior, C. L. *Fuel Process. Technol.* 2003, 82, 167–196.
- [10] Hutson, N. D.; Attwood, B. C.; Scheckel, K. G. *Environ. Sci. Technol.* 2007, 41, 1747–1752.
- [11] Wilcox, J.; Sasmaz, E.; Kirchofer, A. *J. Air and Waste Manage. Assoc.* 2011, 61, 418–426.
- [12] Awasthi, A.; Bhatt, Y. J.; Garg, S. P. *Meas. Sci. Technol.* 1996, 7, 753–757.
- [13] Dujardin, E.; Ebbesen, T. W.; Hiura, H.; Tanigaki, K. *Science* 1994, 265, 1850–1852.
- [14] Chen, J. Y.; Kutana, A.; Collier, C. P.; Giapis, K. P. *Science* 2005, 310, 1480–1483.
- [15] Galashev, A. Y. *Mol. Simul.* 2010, 36, 273–282.
- [16] Kutana, A.; Giapis, K. P. *Phys. Rev. B* 2007, 76, 195444.
- [17] Steckel, J. A. *Chem. Phys. Lett.* 2005, 409, 322–330.
- [18] Padak, B.; Brunetti, M.; Lewis, A.; Wilcox, J. *Environ. Prog.* 2006, 25, 319–326.
- [19] Padak, B.; Wilcox, J. *Carbon* 2007, 47, 2855–2864.
- [20] Huggins, F. E.; Huffman, G. P.; Dunham, G. E.; Senior, C. L. *Energy Fuels* 1999, 13, 114–121.
- [21] Cao, Y.; Li, X. *Adsorption* 2014, 20, 713–727.
- [22] Azamat, J.; Khataee, A.; Joo, S. W. *J. Mol. Graph. Model.* 2014, 53, 112–117.
- [23] Kim, H. W.; Yoon, H. W.; Yoon, S.-M.; Yoo, B. M.; Ahn, B. K.; Cho, Y. H.; Shin, H. J.; Yang, H.; Paik, U.; Kwon, S.; Choi, J.-Y.; Park, H. B.; Bum, H. *Science* 2013, 342, 91–95.
- [24] Galashev, A. Y.; Polukhin, V. A. *Phys. Met. Metallogr.* 2014, 115, 697–704.
- [25] Galashev, A. Y.; Galasheva, A. A. *High Energy Chem.* 2014, 48, 112–116.
- [26] Galashev, A. Y. *Fiz. Mezomekh.* 2014, 17, 67–73.
- [27] Galashev, A. Y.; Polukhin V. A., *J. Surf. Invest. X-ray, Synchr. Neutr. Techn.* 2014, 8, 1082–1088.
- [28] Galashev, A. Y. *Compt. Mater. Sci.* 2015, 98, 123–128.
- [29] Galashev, A. Y.; Rakhmanova, O. R. *Chin. Phys. B* 2015, 24, 020701.
- [30] Galashev, A. Y.; Rakhmanova, O. R. *High Temp.* 2014, 52, 374–380.
- [31] Galashev, A. Y. *High Temp.* 2014, 52, 633–639.
- [32] A. E. Galashev, A. Y.; Polukhin, V. A. *Phys. Solid State* 2013, 55, 2368–2373.
- [33] Galashev, A. Y.; Rakhmanova, O. R. *Phys.–Usp.* 2014, 57, 970–989.
- [34] Galashev, A. Y.; Galasheva, A. A. *High Energy Chem.* 2015, 49, 117–121.
- [35] Zakharchenko, K. V.; Fasolino, A.; Los, J. H.; Katsnelson, M. I. *J. Phys.: Condens. Matter.* 2011, 23, 202202.
- [36] Tersoff, J. *Phys. Rev. Lett.* 1988, 61, 2879–2882.
- [37] Burgos, E.; Halac, E.; Bonadeo, H. *Chem. Phys. Lett.* 1998, 298, 273–278.
- [38] Stuart, S. J.; Tutein, A. V.; Harrison, J. A. *J. Chem. Phys.* 2000, 112, 6472–6486.
- [39] Galashev, A. Y.; Polukhin, V. A. *Phys. Solid State* 2013, 55, 1733–1738.

- [40] Galashev, A. Y.; Dubovik S. Yu. *Phys. Solid State* 2013, 55, 1976–1983.
- [41] Epstein, F.; Powers, M. D. *J. Phys. Chem.* 1953, 57, 336–341.
- [42] Munro, L. J.; Johnson, J. K. *J. Chem. Phys.* 2001, 114, 5545–5551.
- [43] Kutana, A.; Giapis, K. P. *Nano Lett.* 2006, 6, 656–661.
- [44] Schwerdtfeger, P.; Boyd, P. D. N.; Briennes, S.; McFearets, J. S.; Dolg, M.; Liao, M.-S.; Schwarz, W. H. E. *Inorganica Chimica Acta* 1993, 213, 233–246.
- [45] Kim, Y. M.; Kim, S.-C. *J. Korean Phys. Soc.* 2002, 40, 293–299.
- [46] Li, F.-Y.; Berry, R. S. *J. Phys. Chem.* 1995, 99, 2459–2468.
- [47] Ziegler, J. F.; Biersack, J. P.; Littmark, U. *Stopping and ranges of ions in matter*; Pergamon Press: New York, US, 1985; Vol. 1. 321 p.
- [48] Delcorte, A.; Garrison, B. J. *J. Phys. Chem. B* 2000, 104, 6785–6800.
- [49] Lamari, F. D.; Levesque, D. *Carbone* 2011, 49, 5196–5200.
- [50] Wick, C. D.; Martin, M. G.; Siepmann, J. I. *J. Chem. Phys. B.* 2000, 104, 8008–8016.
- [51] Verlet, L. *Phys. Rev.* 1967, 159, 98–103.
- [52] Berendsen, H. J. C.; Postma, J. P. M.; van Gunsteren, W. F.; DiNola, A.; Haak, J. R. *J. Chem. Phys.* 1984, 81, 3684–3690.
- [53] Hafskjold, B.; Ikeshoji, T. *Phys. Rev. E* 2002, 66, 011203.
- [54] Galashev, A. Y. *J. Surf. Invest. X-ray, Synchr. Neutr. Techn.* 2016, 10, 15–22.
- [55] Davydov, S. Yu. *Phys. Solid State* 2012, 54, 875–882.
- [56] Bosio, L.; Cortes, R.; Segaud, C. *J. Chem. Phys.* 1979, 71, 3595–3600.
- [57] Badyal, Y. S.; Bafile, U.; Miyazaki, K.; de Schepper, I. M.; Montfrooij, W. *Phys. Rev. E* 2003, 68, 061208.
- [58] Lobo, V. M. M.; Mills, R. *Electrochem. Acta* 1982, 27, 969–971.
- [59] Rao, R. V. G.; Murthy, A. K. K. *Phys. Status Solidi B* 1974, 66, 703–707.
- [60] Landau, L. D.; Lifshitz, E. M. *Course of Theoretical Physics, Fluid Mechanics*; Nauka: Moscow, US, 1986; Vol. 6, p. 71.
- [61] Eberhart, J. G.; Pinks, V. J. *Colloid Interface Sci.* 1985, 107, 574–575.
- [62] Salla, J. M.; Demichela, M.; Casal, J. *J. Loss Prevent. Proc. Ind.*, 2006, 19, 690–700.
- [63] Hasan, M. N.; Hasan, A.; Ilias, S.; Mitsutake, Y.; Monde, M. *Procedia Engineering* 2014, 90, 618 – 623.
- [64] Ward, C. A.; Stanga, D. *Phys. Rev. E: Stat. Phys., Plasmas, Fluids, Relat. Interdiscip. Top.* 2001, 64, 051509.
- [65] McGaughey, A. J. H.; Ward, C. A. *J. Appl. Phys.* 2002, 91, 6406–6415.
- [66] Lotfi, A.; Vrabec, J.; Fischer J. *Int. J. Heat Mass Transfer* 2014, 73, 303–317.
- [67] Kitamura, H. *J. Phys.: Conf. Ser.* 2008, 98, 052010.
- [68] Duval, M. C.; Soep, B. *Chem. Phys. Lett.* 1987, 141, 225–231.